Observation of impurity accumulation and its compatibility with high plasma performance in W7-X

OPEN ACCESS
IOP Publishing
Plasma Physics and Controlled Fusion
Plasma Phys. Control. Fusion **65** (2023) 105006 (17pp)
https://doi.org/10.1088/1361-6587/acf0e7

Observation of impurity accumulation and its compatibility with high plasma performance in W7-X

D Zhang[1,*], B Buttenschön[1], S Jablonski[2], M Kubkowska[2], O Ford[1], J A Alcusón[3], C D Beidler[1], R Burhenn[1], M N A Beurskens[1], A Langenberg[1], N Pablant[4], F Reimold[1], K Rahbarnia[1], H M Smith[1], Th Wegner[1], G Wurden[5], S A Bozhenkov[1], Y Feng[1], K J Brunner[1], G Fuchert[1], Y Gao[1], J Geiger[1], L Giannone[6], U Höfel[1], M Hirsch[1], Z Huang[7], J Knauer[1], T Kremeyer[1], M Krychowiak[1], S Kwak[1], H P Laqua[1], R Laube[1], U Neuner[1], E Pasch[1], A Pavone[1], A von Stechow[1], J Svensson[1], H Thomsen[1] and the W7-X Team[**]

[1] Max-Planck-Institut für Plasmaphysik, 17491 Greifswald, Germany
[2] Institute of Plasma Physics and Laser Microfusion, 01-497 Warsaw, Poland
[3] Laboratorio de Innovación en Plasmas, Universidad de Córdoba, 14071 Córdoba, Spain
[4] Princeton Plasma Physics Laboratory, Princeton, NJ, United States of America
[5] Los Alamos National Laboratory, Los Alamos, NM, United States of America
[6] Max-Planck-Institut für Plasmaphysik, Garching, Germany
[7] Plasma Science and Fusion Center, MIT, Cambridge, MA 02139, United States of America

E-mail: Daihong.Zhang@ipp.mpg.de

Received 7 July 2023
Accepted for publication 16 August 2023
Published 29 August 2023

Abstract

At the W7-X stellarator, the bolometer system has measured an intensive radiation zone in the inner plasma region (at a normalized radius $\rho \sim 0.3$–0.4) in the hydrogen plasma generated by electron cyclotron resonance heating; it differs from the normal plasma radiation distribution with an edge-localized emission zone. Spectroscopic diagnostics have recorded high-Z elements such as iron. This phenomenon happens in the plasma phases after gas supply turn-off, which results in all impurity relevant diagnostic signals increasing for several seconds. Despite the enhancement of the core radiation, the plasma energy confinement is improved. A transport analysis shows that this impurity radiation behavior is associated with a low diffusion coefficient ($D \sim 0.02$ m^2 s^{-1}) and a reversal of the convection around the radial position of the emission peak, which, under normal conditions, separates the zones of outward convection in the central ($|V| \sim 0.1$ m s^{-1}) and inward convection in the outer region ($|V| \sim 0.3$ m s^{-1}). An impurity accumulation around this radial position has been identified. The transport coefficients obtained are comparable with the theoretical predictions of collisional impurity transport. In the plasma phases studied, both impurity and energy confinement are enhanced. The mechanism responsible for the improvement is believed to be a reduction of micro-instabilities associated with the observed steepening of the density profile, initiated by a low edge plasma density ($<1.0 \times 10^{19}$ m^{-3}) after switching off the gas fueling. The normalized temperature and density gradients fulfil the condition for the suppression of ITG turbulence.

[**] See Klinger *et al* 2019 (https://doi.org/10.1088/1741-4326/ab03a7) for the W7-X Team.
[*] Author to whom any correspondence should be addressed.

Keywords: impurity accumulation, impurity outward convection, impurity inward convection, suppression of ITG turbulence, high plasma performance, plasma radiation, W7-X stellarator

(Some figures may appear in colour only in the online journal)

1. Introduction

Impurity control and energy confinement are topics of crucial importance for achieving high-performance plasmas in both tokamak and stellarator fusion research. It has been observed that the improvement of energy confinement is often accompanied by the accumulation of impurities [1–3], which can limit the discharge duration due to radiative collapse [4, 5]. Therefore, an important goal for fusion experiments is to find operating windows where impurities can be kept at acceptable levels while the plasma is in a high-performance phase, i.e. a matter of handling and controlling both the impurities and the background plasma [6, 7].

In stellarators such as Wendelstein 7-X (W7-X) the magnetic configurations are non-axisymmetric. According to the neoclassical transport theory, the thermodynamic forces acting on the impurity ions will usually support their accumulation in the so-called ion-root regime due to the negative radial electric field ($E_r < 0$). Besides, an electron-root regime with a positive radial electric field ($E_r > 0$) around the plasma center is also expected when the central electron temperature is higher than the ion temperature [8]; then impurities are subject to an outward convection (see also section 5.1). The E_r profiles with transitions from the electron-root to the ion-root have indeed been observed experimentally in W7-X [9]. This suggests that—under certain plasma conditions—impurities can accumulate non-centrally at the radial position where the transition occurs (e.g. under conditions of low turbulent transport). Hence, studying the behavior of impurities, especially in high-performance plasma phases, is of high significance, specifically with regard to the steady-state operational prospects of stellarators.

So far, in the neoclassically optimized W7-X stellarator [10], particle and energy transport have been dominated by turbulent transport, especially in plasmas generated by electron cyclotron resonance heating (ECRH). It is characterized by (1) a transport time of impurities (∼50–100 ms) [11–13] much shorter than predicted by neoclassical theory (∼ several seconds) and (2) an energy confinement time somewhat below the ISS04 stellarator scaling [14, 15]. In addition, the ion temperature T_i is usually limited to 1.5 keV [16, 17], except in some special cases with the T_i-limitation being removed (cf figure 10 [16]). During the gas-fuelled ECRH scenarios (which typically last ∼10 s), no obvious accumulation of impurities has been observed so far. Therefore, the plasma radiation profiles are typically hollow with a peak at the plasma edge associated with intrinsic low-Z impurities (typically carbon and oxygen from the plasma facing components (PFC) at W7-X). This edge-localized radiation zone is advantageous for the life-time of divertor elements, since a stable high-radiation regime with plasma detachment is normally established in high-density plasmas generated by ECRH [18–21].

Recently, plasma phases with prominent radiation from the inner plasma region have been revealed by bolometer tomography [22] in two long-pulse (up to ∼50 s) hydrogen discharges. They are performed shortly after wall boronization during the first divertor operational phase. The radiation intensity at normalized radius $\rho \sim 0.3$–0.4 is comparable to that at the plasma edge ($\rho \geqslant 0.8$) [23]. Spectroscopic diagnostics have demonstrated an increase in the concentration of high-Z impurities (such as Fe). Nevertheless, no thermal collapse of these plasmas occurs; moreover, this plasma phase has a relatively high energy confinement time, which reaches ISS04 scaling [14] (hereafter called high performance (HP) phases); they are among the exceptions as presented and discussed in [16]. We have also observed that this plasma phase has a low edge density that results from switching off the gas supply, which differs from the other high-performance phases initiated by pellet injections [24–26]. Since this is the first observation of such an HP phase in W7-X, we present in detail the evolution from the normal performance (NP) phase to the HP phase. In addition, we have gained insight into the properties of impurity transport through numerical simulations, which show the importance of collisional impurity transport; we also strive to find the mechanisms that lead to improving plasma confinement.

The paper is organized as follows. Section 2 describes the experimental conditions and diagnostic tools; section 3 presents the experimental observations and results; and section 4 examines the impurity transport using the 1D impurity transport code STRAHL [27–29]. Section 5 discusses the collisional transport and the mechanism that suppresses the turbulent transport. Section 6 summarizes the paper.

2. Experimental conditions and applied diagnostics

W7-X is a modular stellarator of the HELIAS (Helical-Axis Advanced Stellarator) type with five-fold symmetry. Five pairs of carbon divertor units are installed periodically in the toroidal direction maintaining stellarator symmetry. These are shown in figure 1. The magnetic field is generated by external non-planar (50) and planar (20) superconducting coils, which allow flexible adjustment of the magnetic configuration. The magnetic configuration in the experiments studied here is the $\iota = 5/4$ island divertor configuration, called 'high-iota'. It features a central magnetic field strength of $<B_0> = 2.43$ T and a monotonically increasing profile of the rotational transform (ι) with values above unity ($\iota_{axis} = 1.01$ at the plasma axis; $\iota_{lcfs} = 1.21$ at the last closed flux surface (LCFS)). The effective minor and major radii are $a = 0.51$ m and $R = 5.51$ m, respectively, and the plasma volume is about 27 m^3, which is slightly smaller than that of the 'standard' configuration (∼30 m^3) with $\iota = 5/5$ island chains at the plasma boundary.

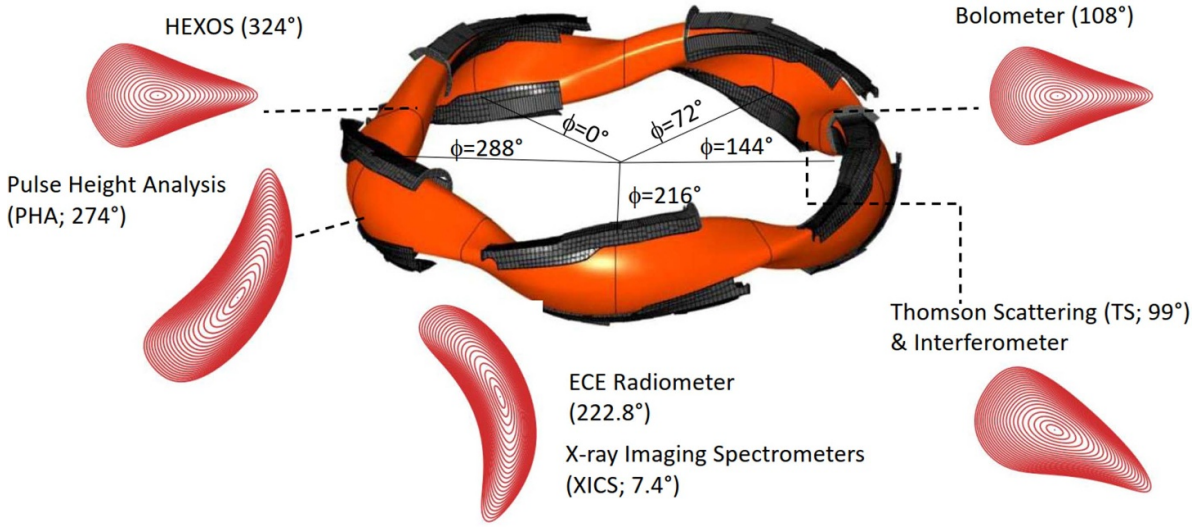

Figure 1. View of the stellarator W7-X with five-fold magnetic topology and the five pairs of symmetrically installed graphite divertor units. The allocation of the selected diagnostic tools, such as the bolometers, the VUV spectrometer HEXOS, and the PHA system for monitoring the impurity radiation, and the ECE, XICS as well as the TS system for measuring the main plasma parameters, at different toroidal positions is shown.

The width of the scrape-off layer (SOL) is ∼8 cm. Compared to the standard configuration, at which most studies have been performed up to now (e.g. [24, 30, 31]), research into 'high-iota' plasmas is still in its infancy.

The plasmas studied here are hydrogen plasmas generated by ECRH in the 2018 experimental campaign (OP1.2b) shortly after wall boronization. Due to a significant reduction in the content of oxygen impurities, carbon released from the divertor targets is the main intrinsic impurity. Other impurities such as Cl and S and also some high-Z elements (such as Fe, Cu, and Cr) have occasionally been observed. They are associated with ingredients contained in the PFCs. To study impurity transport, iron had been injected in previous experimental days by laser blow-off (LBO) [32] and tracer-encapsulated solid pellets [33]. It was also deposited onto the PFCs and could have served as an additional source of impurities.

One of the key diagnostic methods relevant to this work is the bolometer system located around a toroidal position $\phi = 108°$ (>2 m away from the plasma wall interaction region on the divertor targets). It consists of a horizontal (HBC) and a vertical (VBC) pinhole camera [34], viewing the triangular plasma cross section (see figure 1) from the outboard side and the bottom of W7-X, respectively. The line-of-sight (LoS) distribution, together with the Poincaré-plot of the 'high-iota' magnetic configuration is shown in figure 2. The typical time resolution of the system is ∼0.8–1.6 ms. The main detector arrays are of metal resistive type with blackened gold absorbers to measure the total radiated power loss P_{rad} from the plasma and to provide 2D radiation intensity profiles. The P_{rad} values are calculated by linear extrapolation of the radiated power falling within the field of view (FoV) of the HBC (due to its good LoS coverage over the plasma cross section) to the total plasma volume (neglecting toroidal variation) [18]. The 2D radiation intensity profiles are obtained from tomographic reconstructions using the relative gradient smoothing

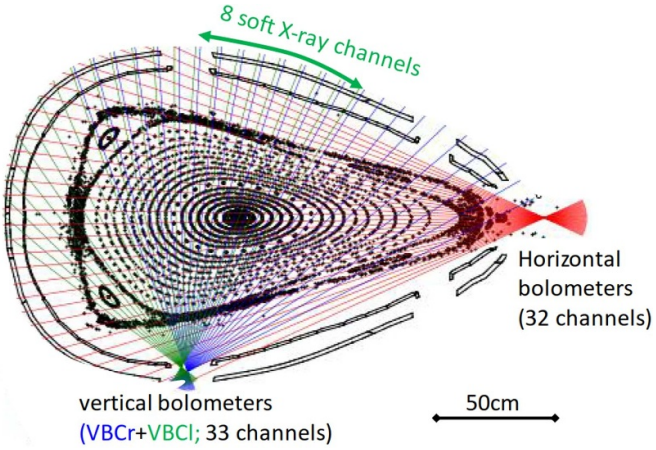

Figure 2. The LoS distribution of the HBC (32 channels) and VBC (consisting of VBCr and VBCl with 24 channels each) around the triangular plasma cross section ($\phi = 108°$) at W7-X. The LoS of 8 SXR-channels in the sub-bolometer camera VBCl through the plasma center are labeled accordingly. The high-iota magnetic topology with four interlinked magnetic islands in the SOL is depicted by the Poincaré plot.

method. Details can be found in [22]. In addition, there are some detectors covered with a 12 μm Be optical filter to measure the emission fraction of soft x-rays (SXR; >500 eV) from the plasma core. Being sensitive to line emission from high-Z elements, they are suitable for studying the transport of high-Z impurities [35].

The high-efficiency extreme ultraviolet overview spectrometer (HEXOS) [36] is used for identifying impurity elements. It measures the line emission (not absolutely calibrated) of impurity ions using four individual spectrometers covering the spectral range between 2.5 nm and 160 nm. The temporal resolution of the system is 1.0 ms. Its single LoS crosses the

plasma center in another equivalent triangular cross section two field periods away from the bolometers (see figure 1).

Another important diagnostic tool is the pulse height analysis (PHA) system [37]. It consists of three independent energy channels that record SXR spectra in three different ranges (1.5–19.6 keV, 0.9–19.6 keV, and 0.5–19.6 keV) to detect and track the evolution of low-Z (such as carbon, oxygen, and nitrogen), medium-Z (such as sulfur, chlorine, and argon), and high-Z (such as chromium, iron, nickel, and copper) impurities. Silicon drift detectors (SDDs) with different optical filters (e.g. a thin polymer window and beryllium foils of different thickness) are used. The system has sufficient energy resolution (e.g. 150 eV FWHM at 5.9 keV), moderate temporal resolution (50–100 ms), and a spatial resolution of 2.5 cm. The line of sight crosses near the plasma center at the toroidal position $\phi = 274°$ (see figure 1). Based on the line-integrated measurements of the SXR spectra, which are absolutely calibrated [37], the intensity of the impurity ions can be derived alongside the identification of the impurity element by comparing the experimental results with modeled spectra (using an updated RayX code) [38]. Subsequently, the ion effective charge $Z_{\rm eff}$ can also be obtained. It agrees with the line-averaged $Z_{\rm eff}$ determined by the visible spectrometer, which has a single line of sight through the plasma core [39], within diagnostic uncertainties of ∼0.5 (see figure 7).

Charge-exchange recombination spectroscopy (CXRS) [40] using a high-resolution spectrometer can provide CVII density profiles based on visible CVI line (at 529.07 nm) measurements via active charge-exchange (CX). This normally requires a short neutral beam injection pulse (NBI 'blips'), which, however, has not been performed for the discharges studied here. The line-integrated passive measurements implicitly contain useful information about impurity transport. But the LoS of the system has a much broader toroidal extent (ϕ from 77° to 150°) with an extremely long LoS (∼several meters), which complicates the interpretation of the measurements. This is mainly due to the 3D distribution of the neutral hydrogen pressure P_0 in W7-X. For example, in the toroidal positions bounded by divertor targets, a high P_0 value and hence a high density of neutral hydrogen is expected [41, 42], which can cause a pronounced CX effect that makes comparison with bolometer results difficult. The CXRS measurements are therefore not presented in this work.

The background plasma parameters, such as the stored energy $W_{\rm p}$ and the line-integrated density $<n_{\rm e}>$, are provided by a compensated diamagnetic loop [43] and an interferometer system, respectively. The electron density $n_{\rm e}$ and temperature $T_{\rm e}$ profiles are obtained by the Thomson scattering (TS) system [44, 45], and the density profiles are cross-calibrated with the interferometer data because the absolute density calibration of the TS diagnostic was lost in this campaign due to misalignment of the laser. In addition, electron temperature time traces are obtained from the electron cyclotron emission (ECE) measurements [46, 47]. Information on the ion temperature $T_{\rm i}$ and the radial electric field $E_{\rm r}$ is provided by the x-ray imaging crystal spectrometer (XICS) [9, 48]. The uncertainties in the $T_{\rm i}$ (up to 0.3–0.5 keV) and $E_{\rm r}$ measurements (up to 2 kV m^{-1}) depend on the emissivity of Ar^{16+}, as the XICS diagnostic measures the Doppler broadening and Doppler shift of characteristic emission lines; argon is introduced into W7-X at trace levels for this diagnostic purpose and the emissivity is dependent on the argon density as well as the electron density and temperature.

3. Experimental observations

The discharges studied are XP20180808.5 and XP20180808.7 (hereafter referred to as XP5 and XP7, respectively). Both plasmas are initially generated by 1.2 MW ECRH and maintained by half the power in the later phase. During the discharges, gas fueling is alternately turned on and off via feedback control to stabilize the plasma density $<n_{\rm e}>$. Figure 3 shows the time traces of the plasma parameters (a)–(d) for XP5 and (e)–(h) for XP7. We made the following observations.

3.1. Buildup of HP-phases and parameter profile evolution by the impact of gas puff

As mentioned in the Introduction, the HP phase is referred to the plasma phase that has a confinement time $\tau_{\rm E}$ comparable to ISS04 scaling, i.e. $\tau_{\rm E}/\tau_{\rm ISS04} \sim 1$. We present two discharges because the transition to the HP phase occurs at different ECR heating powers but for the same reason, namely, turning off the gas supply. This shows the robustness of the observations. In the following, the energy confinement time is calculated using $\tau_{\rm E} = \frac{W_{\rm p}}{P_{\rm ECRH} - {\rm d}W_{\rm p}/{\rm d}t}$ and $\tau_{\rm ISS04}$ is the energy confinement time predicted by ISS04 scaling [14], i.e. $\tau_{\rm ISS04} = 0.134 a^{2.28} R^{0.64} P^{-0.61} n_{\rm e}^{0.54} B^{0.84} \iota_{2/3}^{0.41}$, using $a = 0.51$ m, $R = 5.51$ m, $B = 2.39$ T (the volume-averaged value), and $\iota_{2/3} = 1.1$; $P = P_{\rm ECRH}$ and $n_{\rm e} = <n_{\rm e}>$ are varied during the experiments.

3.1.1. Transition from NP- to HP-phase

- In XP5, the gas puff is automatically turned off by feedback control at $t = 16.0$ s shortly after $P_{\rm ECRH}$ had been reduced (see the first vertical dashed line in figures 3(a)–(d)) as the value of $<n_{\rm e}>$ (∼0.23×10^{20} m^{-3}) reaches the target value. The decrease in $P_{\rm ECRH}$ causes the core electron temperature $T_{\rm e}(0)$ (labeled Te_ECE13), the ion temperature $T_{\rm i}(0)$ (line-averaged value from the central XICS channel) and the plasma stored energy $W_{\rm p}$ to decrease, but they increase again after the gas puff is turned off. After another ∼3.0 s (marked by the second vertical dashed line), the plasma stabilizes and reaches the HP phase, where both $W_{\rm p}$ and $T_{\rm i}(0)$ have a slightly higher value (although the $P_{\rm ECRH}$ is halved!). This leads to an energy confinement time $\tau_{\rm E} = 0.4$ s and a ratio of $\tau_{\rm E}/\tau_{\rm ISS04} \sim 1$, which are higher than $\tau_{\rm E} = 0.2$ s and $\tau_{\rm E}/\tau_{\rm ISS04} = 0.7$ in the plasma phase ($t < 16.0$ s) with NP. After transition to the HP-phase, the value of $T_{\rm i}(0)$ reaches ∼1.7 keV and $<n_{\rm e}> \sim 0.3 \times 10^{20}$ m^{-3}; both parameters show a distinct increase. The total radiation loss $P_{\rm rad}$ initially decreases as $P_{\rm ECRH}$ decreases, but then returns to a value comparable to that before ECRH power reduction, yet has a higher radiation loss fraction $f_{\rm rad} = P_{\rm rad}/P_{\rm ECRH} \sim 45\%$. The

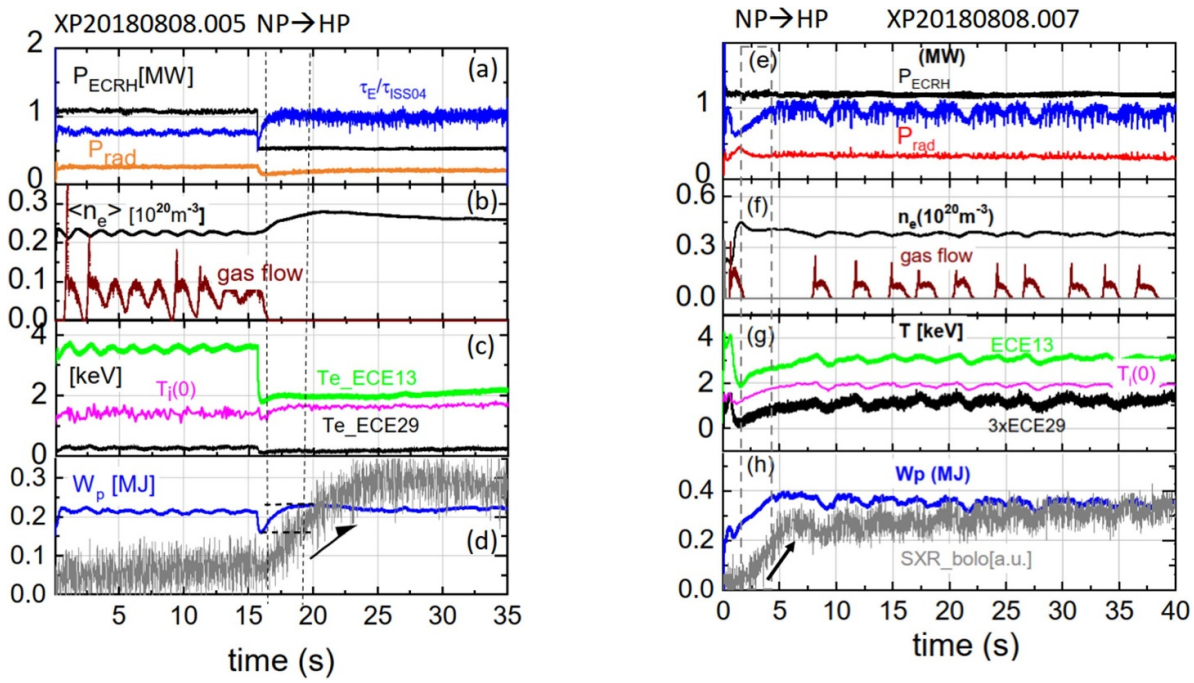

Figure 3. Time traces of the relevant diagnostics for XP5 (a)–(d) and XP7 (e)–(h). From top to bottom: P_{ECRH}, P_{rad}, $<n_{\mathrm{e}}>$, gas-flow, $T_{\mathrm{e,core}}$ and $T_{\mathrm{e,edge}}$ from ch13 and ch29 of the ECE diagnostic (note that the signal from ECE29 in (g) is magnified by a factor 3 for clarity), $T_{\mathrm{i}}(0)$ from the central channel of XICS, the plasma stored energy W_{p}, the soft-x-ray from SXR-channel in the bolometer system. The rise of the SXR level is indicated by arrows (in black). The dashed frames are the time intervals from switching off the gas flow to reaching the W_{P} plateau (i.e. the transition from the NP to the HP phase).

SXR signal increases substantially by a factor of ∼6 reaching a plateau (at $t = 24.0$ s) ∼5 s later than W_{p}. Since the main plasma parameters remain rather constant, the increase in the SXR signal is attributed to a change of impurity transport. A transport time $\tau_Z \sim 5$ s is estimated, which is much longer than the typical impurity transport time in conventional plasmas (∼50–100 ms) but comparable to neoclassical predictions (see section 5.1).

- In XP7, the first gas puff is applied after the plasma start-up and is switched off at $t = 1.7$ s. From then on until 4.0 s (marked by a dashed frame in figures 3(e)–(h)), W_p increases, as do the electron temperatures, both $T_{\mathrm{e}}(0)$ (ECE13) and $T_{\mathrm{e,edge}}$ (ECE29), and the central ion temperature $T_{\mathrm{i}}(0)$. The value of $T_{\mathrm{i}}(0)$ gradually approaches 2.0 keV. A quasi-stationary HP phase is first reached at $t \sim 4.0$ s, with a value of $\tau_{\mathrm{E}} = 0.35$ s and $\tau_{\mathrm{E}}/\tau_{\mathrm{ISS04}} \sim 1$. It continues for a few seconds until the next gas puff (at $t \sim 8.0$ s). Consequently, W_{p} decreases, as do the electron and ion temperatures, indicating the back-transition to an NP phase. This phenomenon repeats several times when the gas supply is turned on and off sequentially; it takes about 40 s until the P_{ECRH} is reduced. Thereafter, the gas supply is turned on continuously and the plasma stays in an NP phase (this phase is not further investigated in this work and is therefore not shown in figures 3(e)–(h); details can be seen in figure 3 in [23]).

Similar to XP5, the SXR emission (see figure 3(h)) increases steadily during the initial buildup of the HP phase. It reaches its plateau at $t = 6.0$ s, ∼2.0 s later than W_{p}, again indicating a long transport time of impurities. Throughout the discharge, the SXR level shows a strong correlation with the W_{p} variation in response to external gas puffing.

It is noteworthy that in the HP phases for both discharges, the ECE channels viewing the outer plasma region have observed T_{e}-bursts with an inversion postion at $\rho \sim 0.7$–0.8. The bursts occur in an irregular time interval (∼25 ms) accompanied by a small drop in the Wp value (by a factor of ∼2%). This is hidden in the time trace of Wp in figures 3(d) and (h), but appears as a distinct fluctuation in the calculated confinement time ratio $\tau_{\mathrm{E}}/\tau_{\mathrm{ISS04}}$ due to the dWp/dt term (see figures 3(a) and (e)). Some edge bolometer channels, as well as diagnostics that measure emission from CVI, record visible fluctuations (see later figures 7(c) and (g)). This behavior, which resembles ELMs in H-mode tokamak plasmas [49], has also been observed in W7-X plasmas in other magnetic configurations [50]. The report on edge plasma fluctuation in XP5 can be found in [51]. However, our concern here is with impurity transport in the core region and therefore we will not discuss it further.

3.1.2. Parameter profile evolution. The way of gas puffing during the discharges XP5 and XP7 shows clear effects on plasma parameters. We select two time points for each discharge to show the profile variation from NP to HP phases. The n_{e} and T_{e} profiles measured with the TS system (with typical error bars of $\Delta n_{\mathrm{e}} \sim 5 \times 10^{18}$ m^{-3} and $\Delta T_{\mathrm{e}} \sim 20$–$50$ eV) and their fits are depicted in figure 4 as a function of the normalized radius $\rho \equiv r_{\mathrm{eff}}/a$, where the effective radius is defined

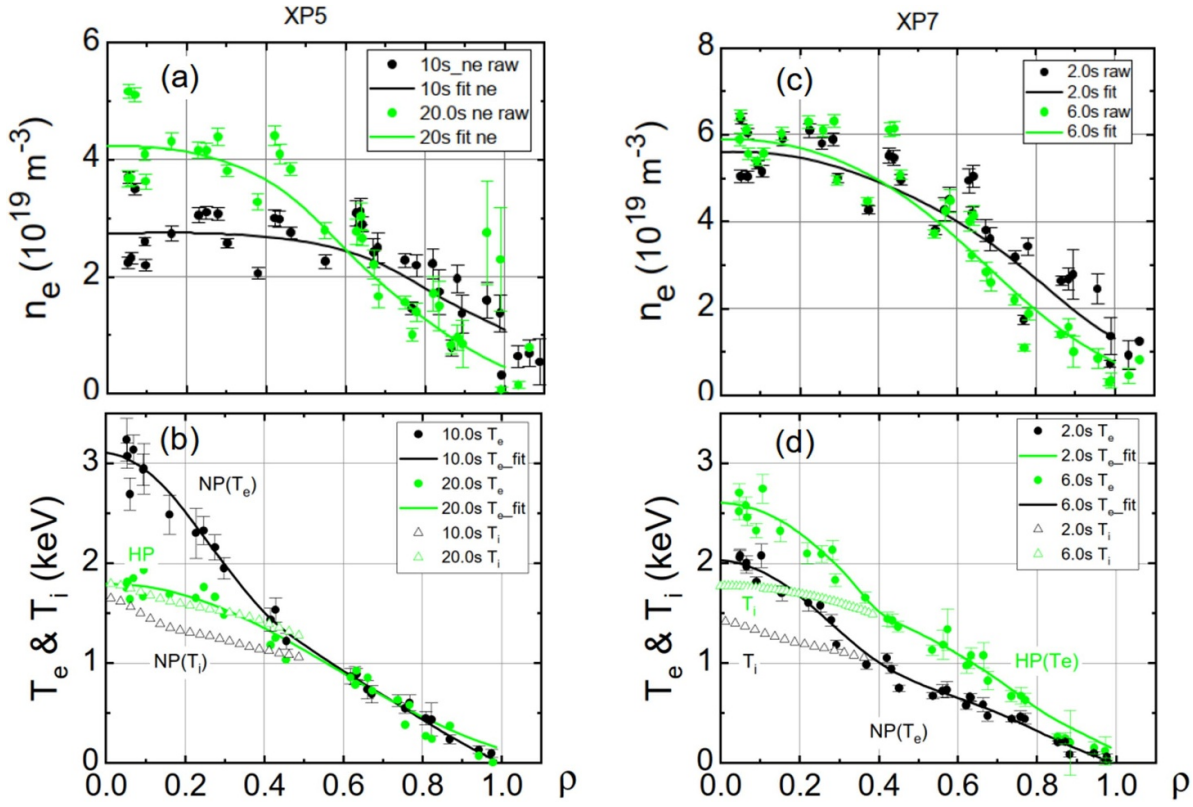

Figure 4. The T_e and n_e-profiles obtained by the TS system for the selected time points in the NP (in black) and HP (in green) phases for XP5 (a), (b) and XP7 (c), (d). The T_i profiles from the XICS system are also shown but not fully plotted due to the large uncertainty in the plasma region with relatively low T_e, which usually leads to an overestimation of T_i.

by $r_{\text{eff}} = \sqrt{\frac{\bar{A}}{\pi}}$, with $\bar{A}$ the average poloidal flux-surface area. The transition to the HP phases is accompanied by a significant decrease in the edge density ($n_{e,\text{lcfs}} < 1.0 \times 10^{19}$ m^{-3}) and a peaking of the n_e profiles. Note that $n_{e,\text{lcfs}} > 1.0 \times 10^{19}$ m^{-3} in the NP phase. As for the electron temperature, the HP phase in XP5 has a relatively low value in the plasma center with $T_e(0) = 2.0$ keV, which is ∼1.5 keV lower than in the NP phase; this is due to the reduction of P_{ECRH} from 1.2 MW to 0.6 MW. In contrast, in XP7 (constant $P_{\text{ECRH}} = 1.2$ MW), the T_e profile in the HP phase is fully developed, with $T_e(0)$ reaching 2.6 keV.

The T_i profiles measured with XICS are also shown there. For the plasma regions where T_e is rather low (<1.0–1.5 keV), the uncertainty of the T_i value is large (up to ∼0.5 keV), which is related to the weak Ar^{16+} line emission (see section 2). This can lead to an apparent $T_i > T_e$ in the outer plasma region, in which case the T_i values are replaced by T_e values since these cases are considered unphysical (not like in NBI discharges, for which this is indeed feasible), since in ECRH discharges all the heating power is deposited in the electrons and then transferred to the ions via collisions. We thus show the T_i values only for the inner radial positions, where $T_i \leqslant T_e$. This leads to a problem when using XICS profiles in section 5 since the two profiles do not connect seamlessly, leading to discontinuities in the a/L_{Ti} values (see figure 12(left)).

Therefore, to achieve a smooth coupling with the T_e profile from the TS system, some data points in the XICS data are required to be adjusted near the connection position (at $\rho = 0.4$–0.5) (see [52]). This is done for the collisional impurity transport analysis in section 5.1.

3.2. Impurity behavior

3.2.1. Radiation profile evolutions. The high SXR emissions in the HP phases of XP5 and XP7 shown in figure 2 originate from deep within the confined plasma region. This is obtained for the first time by bolometer tomography [16] for ECR-heated plasmas. The 2D emission patterns for the HP phases using the example of $t = 20.0$ s in XP5 and $t = 6.0$ s in XP7 (see figure 3) are shown in figures 5(a) and (c). They clearly show a distinct radiation zone in the inner plasma region with the addition of an edge-localized radiation zone. For comparison, the NP phases at $t = 10.0$ s in XP5 and $t = 2.0$ s in XP7 are shown in figures 5(b) and (d), respectively; only the edge-localized radiation pattern characterized by poloidal asymmetry (which normally occurs in the ECRH-generated plasma [53]) appears.

In figures 6(a) and (b), we show the evolution of the radial 1D radiation profile for XP5 and XP7, respectively; they are obtained by poloidal averaging of the 2D profiles from tomographic reconstructions, some of which are shown in figure 5. In the SOL ($r_{\text{eff}} > a$), an extrapolation of the LCFS has been made (see [22]). The progressive peak of the radiation profile in the inner plasma region ($r_{\text{eff}} < 30.0$ cm, i.e. $\rho < 0.6$) corresponds to the increase in the SXR signal shown in figure 3. For

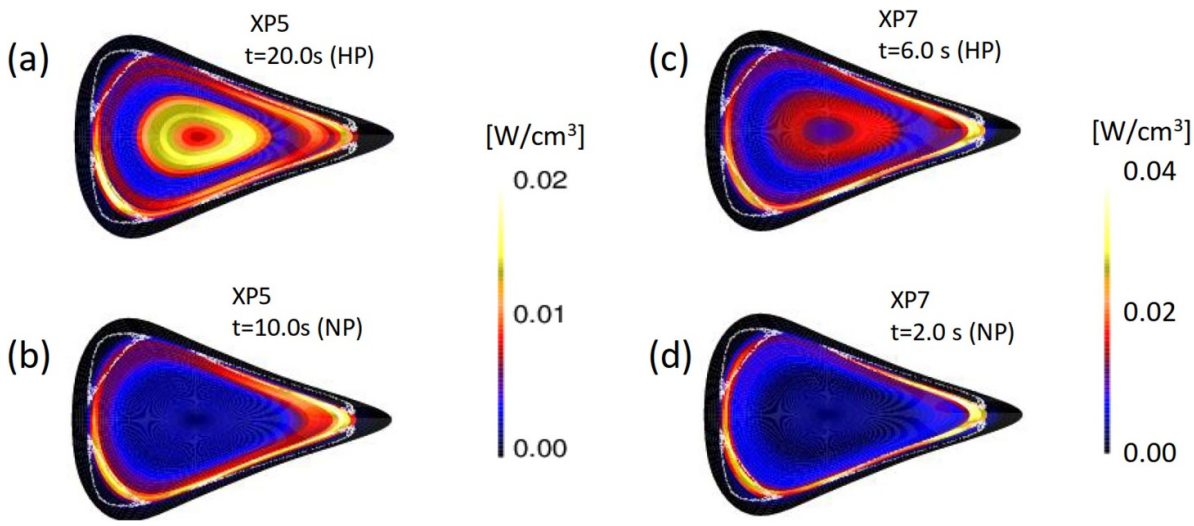

Figure 5. The 2D emission patterns obtained by bolometer tomography for selected time points in the NP and HP phases for XP5 (a), (b) and for XP7 (c), (d), respectively.

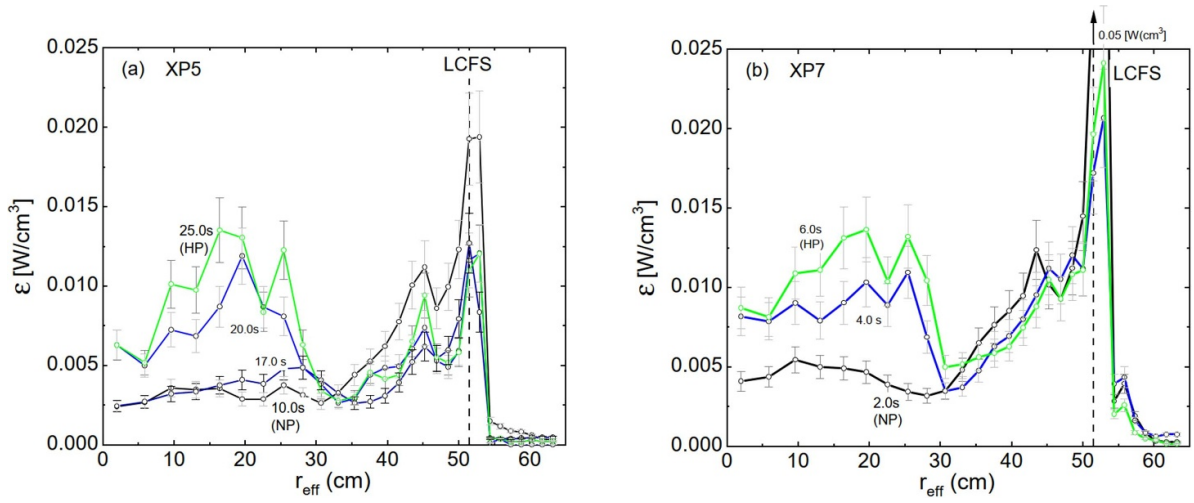

Figure 6. The time evolution of the radial profile of the radiation intensity in XP5 (a) and XP7 (b), obtained by poloidal averaging of the 2D emission profiles (see figure 5), again shows the prominent radiation zone in the inner region $r_{\rm eff} < 30.0$ cm (i.e. $\rho < 0.6$). The green curves show the cases with stabilized impurity transport in the HP-phases.

the HP phases in both plasmas studied (see the green lines), the maximum emission values there are close to each other ($\varepsilon_{\rm m} \sim 15.0$ mW cm^{-3}); they are located at a slightly different radial position, $\rho \sim 0.3$ for XP5 and $\rho \sim 0.4$ for XP7. This similarity is mainly related to the similar local plasma temperature ($T_{\rm e} \sim 1.5$ keV) for both plasmas and the same high-Z impurity ions (see later figure 7). In addition, we can see a small emission 'hole' around the plasma axis whose local emissivity is weaker than the maximum emissivity by a factor of ∼2.0–2.3.

3.2.2. Impurity species and accumulation. The presence of high-Z elements (such as Fe and Cr) is confirmed by the HEXOS and PHA measurements. From the data analysis of the PHA system, FeXXV is the dominant impurity ion. Other elements such as C, O, S, and Cl, as well as Ar (for XICS diagnostic purposes) are also detected. The C element is used for further analysis in the following sections (although the absolute concentration is not known). Oxygen and other elements are ignored as their amounts are low after wall boronization.

The time traces of the diagnostics recording the impurity radiation are collected in figure 7 ((a)–(d) for XP5 and (e)–(h) for XP7). Only the time interval concerning the transitions from the NP to the HP phase is displayed. After turning off/reducing the gas supply, the signals from the bolometer core channel (e.g. with LoS through $\rho = 0$ and $\rho = 0.3$) increase significantly ($t > 16.5$ s for XP5 and $t > 2.0$ s for XP7). This is in agreement with the time traces of the line emission of FeXXII with $Z = 21$ (13.6 nm) and CVI with $Z = 5$ (3.3 nm) measured by the HEXOS system. In contrast, the emission of

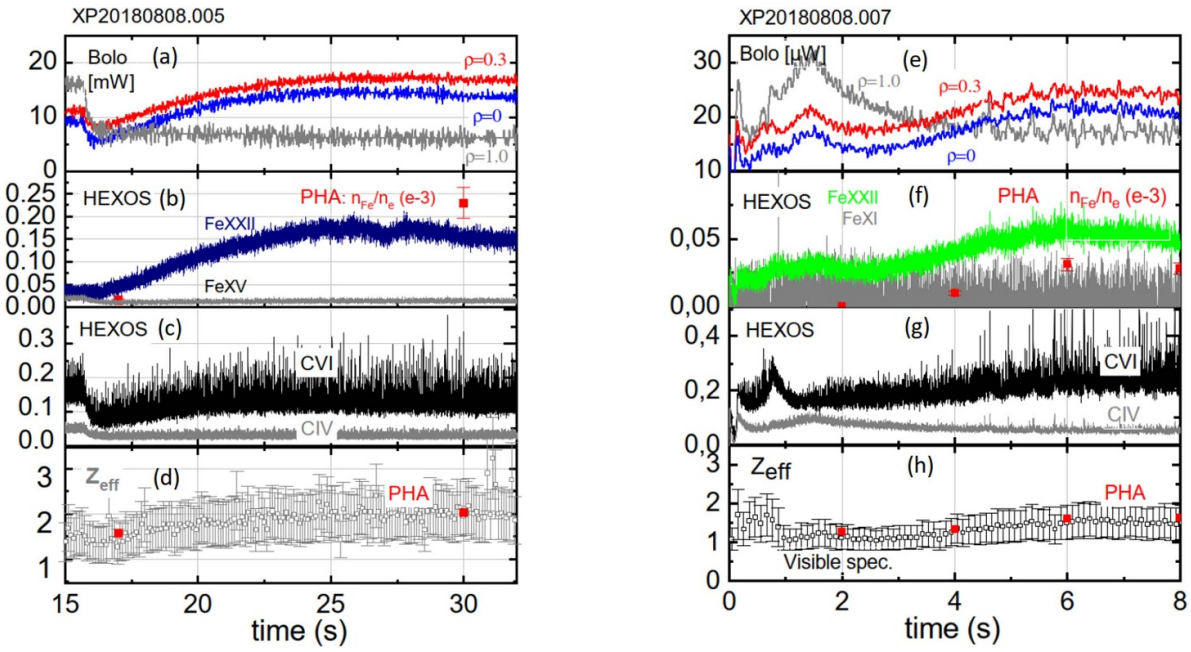

Figure 7. Time traces of impurity-related diagnostics for XP5 (a)–(d) and XP7 (e)–(h). From top to bottom: the signals of the bolometer channels viewing the plasma center ($\rho = 0$ in blue and $\rho = 0.3$ in red) and -edge ($\rho = 1.0$ in grey), the estimated Fe-concentration $n_{\mathrm{Fe}}/n_{\mathrm{e}}$ from the PHA system (red squares), the line emission of impurity ions, FeXXII ($Z = 21$) and CIV ($Z = 3$) from HEXOS, the averaged Z_{eff} from visible spectroscopy (grey symbols) and that estimated by the PHA system (red squares).

low-charged states, such as FeXI with $Z = 10$ (18.0 nm) and CIV with $Z = 3$ (41.9 nm), remains at their level or decreases, as does the edge bolometer channel ($\rho = 1.0$). The results of the estimated Fe concentration $n_{\mathrm{Fe}}/n_{\mathrm{e}}$ from the PHA system for selected time points (red squares) are superimposed on the (uncalibrated) HEXOS data. The value of $n_{\mathrm{Fe}}/n_{\mathrm{e}}$ reaches $\sim 2.5 \times 10^{-4}$ for XP5 and $\sim 0.4 \times 10^{-4}$ for XP7 in the HP phase (while it is undetectable in the NP phase). Accordingly, the effective ion charge Z_{eff} reaches up to ~ 1.9 in XP5 and ~ 1.6 in XP7 in the HP phase. The results from the PHA system and the visible bremsstrahlung measurements show good agreement (see figures 7(d) and (h)). All these together suggests that the impurities possibly accumulate in the high-temperature core. The rise time of these signals is on the order of seconds for both plasmas and is consistent with the SXR channel signals shown in figure 3.

It is worth noting (1) that the signals from the bolometer channel with the LoS through the plasma center ($\rho = 0$) are a fraction weaker than those from the channel with the LoS through $\rho = 0.3$ ($\sim$15 cm from the center) for both plasmas studied, which is related to the lower emission around the plasma axis in the radiation profiles. This phenomenon is different from the one observed in purely NBI-heated W7-X plasmas, where a central emission peak is observed, reflecting a different feature of impurity transport. A comparison of impurity transport and radiative behavior between ECR and NBI heated plasmas will be presented elsewhere. (2) The CVI line emission in both XP5 and XP7 shows stronger fluctuations (see figures 7(c) and (g)). This is also observed in some edge bolometer channels. We believe that this is related to the T_{e}-bursts in the outer plasma region accompanied by a small W_{p} reduction (ELM-like behavior) (see section 3.1). However, this phenomenon is not the subject of this work.

4. Numerical simulations of impurity radiation profile

4.1. General considerations

The local emissivity $\varepsilon(r)$ from impurity (element X) with atomic number Z_0 is proportional to the local impurity density n_X and electron density n_e, i.e.,

$$\varepsilon_{\mathrm{rad}} = n_{\mathrm{e}} n_X L_X \left(Z_0, T_{\mathrm{e}}\right), \tag{1}$$

where L_X is the radiative power-loss function of the impurity [54]. It relates to the fractional abundance of ions of charge Z ($Z = 0,\ldots,Z_0$) and the 'radiative power-loss coefficient' P_z, which includes the power loss due to the leading lines, the recombination cascade power loss due to the recombination of this ion, and the bremsstrahlung loss.

The radiation profile measured by the bolometer system contains therefore information about the impurity transport. By simulating the radiation profile, the impurity transport characteristic can be determined.

Impurities in W7-X are first subject to transport in the 3D SOL after being released from the wall. Since there is no closed flux surface (FS) in the SOL, a numerical tool such as the EMC3-Eirene code [55] is usually required to solve the 3D edge impurity and neutral transport. The complexity of the non-uniform emission pattern at the plasma edge is also evident from the 2D distribution in figure 5, which reflects a

non-uniform impurity density distribution in the poloidal direction. In addition, asymmetry of impurities on the FS is also possible, related either to electrostatic potential variations on the FS [56, 57] or to frictional forces between impurity- and background ions based on the neoclassical theory of parallel transport of impurities [58]. The latter has been pointed out and confirmed by the radiative asymmetry in the outer plasma region in W7-X (see [22]). However, our concern is to understand the impurity cross-field transport in the inner confined plasma region. Therefore, we ignore all these asymmetries and assume that all plasma parameters and the impurity density are uniformly distributed on a FS.

Hereafter, the simplified 1D impurity transport code STRAHL [28, 29] is used. It calculates the spatiotemporal evolution of the FS-averaged impurity ion density $<n_z>$ (hereafter referred to as n_z) by solving the coupled equation for all ionization states Z of a selected impurity species

$$\frac{\mathrm{d}n_z}{\mathrm{d}t} + \frac{1}{r}\frac{\mathrm{d}}{\mathrm{d}r}(r\Gamma_z) = -(n_e S_z + n_e R_z + n_H \alpha_z^{cx}) n_z + n_e S_{z-1} n_{z-1} + \left(n_e R_{z+1} + n_H \alpha_{z+1}^{cx}\right) n_{z+1}. \quad (2)$$

Here, $\Gamma_z = -D(r)\,\mathrm{d}n_z/\mathrm{d}r + V(r)\,n_z$ is the impurity flux composed of a diffusive and a convective part with *D(r)* and *V(r)* standing for the diffusive and convective transport coefficients, respectively. S_Z and R_Z are the ionization and recombination rate coefficients, respectively, for the corresponding ionization state Z; α_z^{cx} is the recombination coefficient due to charge exchange; they are all taken from the ADAS database [54]. The density of neutral impurity particles in the plasma boundary decays as $n_0(r) = n_0(r_w)\frac{r_w}{r}\exp(-\int_r^{r_w}\frac{n_e S_0}{v_0}\mathrm{d}r)$, with ν_0 denoting the thermal velocity of the neutrals released from the wall with a kinetic energy of E_0 (set to 5.0 eV in the simulations). Thereby, the temporal evolutions of $n_z(r,t)$ are obtained. Subsequently, the local radiation intensities are calculated based on equation (1). The necessary 'radiative power-loss coefficients' are also obtained from the ADAS database.

When initializing the transport coefficients for the STRAHL calculations, the following aspects are considered.

4.1.1. The impact of the normalized convection parameter V on profile peaking.* In the source-sink free region, the impurity density profile $n_X(r)$ is determined exclusively by the ratio of convection parameter and the diffusion coefficient for given plasma conditions. It reads [59]:

$$n_X \propto \mathrm{n}_{X,0} e^{-\int_r^{r_0}\frac{V(\tilde{r})}{D(\tilde{r})}d\tilde{r}}, \quad (3)$$

where $n_{X,0}$ is the impurity density at the outer source-free radial position r_0, (e.g. at the LCFS), which is associated with the neutral impurity flux density originating from the wall Γ_0 and the impurity transport in the edge. Thereafter, we consider a normalized convection parameter V^*, which is defined as $V^*(r) = V(r)/D(r)$ due to its direct influence on the impurity density profile. This results in

$$\frac{1}{n_X}\frac{\mathrm{d}n_X}{\mathrm{d}r} = V^*. \quad (4)$$

Three simple n_X-profiles are shown by equation (4) directly: (1) flat for $V^* = 0$ (no convective transport), (2) peaked around the plasma axis for $V^* < 0$ (inward convection), and (3) hollow for $V^* > 0$ (outward convection). If the n_X-profile peaks at a certain radial position $r = r_\mathrm{p}$, then we expect $V^*(r_\mathrm{p}) = 0$. Note that $V^*(0) \equiv 0$.

The peak in the radiation profile (with $\mathrm{d}\varepsilon_\mathrm{rad}/\mathrm{d}r = 0$) will be strongly correlated with the n_X profile, hence the V^* profile. Tests about the sensitivity of the ε_rad profile, for both C and Fe element, to the V^* profile have been carried out. Their results (inclusive the summation over the two elements) are shown in figures 8(a) and (c), and the corresponding V^* profiles are shown in figures 8(b) and (d). In the simulations, the *D(r)* profile and the value V^* at $\rho = 1.0$ are fixed; the V^* profile variation is achieved by adjusting the value at the selected radial positions (i.e nodes; see the circles in figures 8(b) and (d)). The background plasma parameters and the influx of C and Fe impurities are the same as those used in the XP7 simulation in section 4.2. It can be seen that (1) the peak of ε_rad in the inner plasma region (see figure 8(a)) disappears when the V^* profile becomes flat (e.g. $V^* \sim 0$), as shown in (b); (2) the position of the peak shifts toward the plasma center when the V^* values are all negative in the profile. These results show how sensitive the impurity radiation peak is to the position of the V^* reversal in the profile.

*4.1.2. The impact of V * and D on the impurity confinement time τ_z.* The impurity confinement time $\tau_z$is a function of the transport coefficients V^* and D, and the plasma minor radius a for the impurity in the plasma center. The relationship is roughly expressed as below [59]

$$\tau_z \approx 0.173\, e^{-0.17(aV^*/\rho)} a^2/D, \quad (5)$$

where the expression in the parenthesis (also called drift parameter) is assumed to be a constant. The buildup or transport time for impurities to reach the plasma center after being released from the wall is related to the value of τ_z. It is increased with pure inward convection ($V^* < 0$) and decreased with pure outward convection ($V^* > 0$). Also, it is inversely proportional to the D value at fixed drift parameter.

Next, we consider the rise time of the SXR signal, which is related to the time of impurity transport. This signal is calculated using the SXR emissivity (in W m^{-3}) for C and Fe and the main plasma, taking into account the optical transmission of the 12 μm Be filter (see [60]) and the actual LoS geometry.

4.2. STRAHL simulations and results

In the following, the simulations for XP7 are presented in detail.

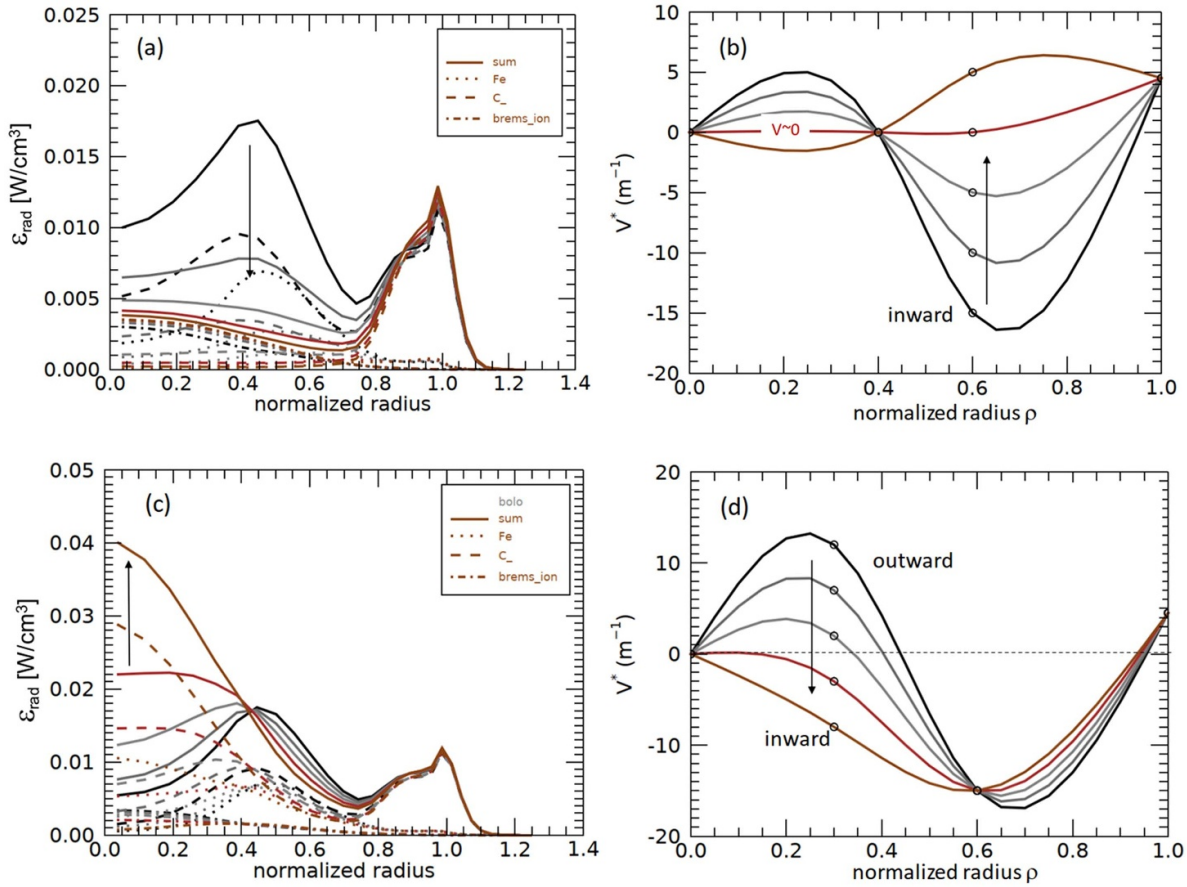

Figure 8. Demonstration of the influence of the normalized convection parameter V^* on the radiation profiles from C (in dashed line) and Fe (in dotted line) ions; their summation is shown as solid line. (a) The disappearance of the peak in the inner plasma region when the V^* profile becomes flat, as shown in (b); (c) the position of the peak shifts toward the plasma center when the V^* values for $\rho < 0.5$ change their sign from positive to negative. The arrows show the response of ε_{rad} peak to the variations of the local V^* value (i.e. the nodes marked with circles).

4.2.1. Input parameters. The T_e and n_e profiles within the LCFS are from the TS measurements; and three key time points, i.e. ∼2.0 s (just after the gas puff is turned off), ∼4.0 s (when W_p reaches its plateau), and ∼6.0 s (when the SXR signal reaches its plateau) are considered. The values for $t = 2.0$ s and 6.0 s are shown in figures 4(c) and (d), whereas those for $t = 4.0$ s are not shown because they are very similar to those at 6.0 s. A radial exponential decay of the parameters is assumed in the SOL since T_e and n_e values are experimentally not available there; a decay length of ∼2.5 cm is used. When modeling the particle flux in the SOL, STRAHL considers a connection length, Lc, and a parallel flow velocity into the divertor. The flow velocity is set to a Mach-number of 0.2, while $Lc = 100$ m is used. For the neutral hydrogen density n_H, STRAHL requires its complete profile. The actual neutral density in W7-X is a complex 3D function and varies strongly in the toroidal direction; it has a maximum value near the strike lines on the divertor targets (here the high-iota tail) and a minimum around the triangular cross-section (>2 m away from the divertor target). Based on the EMC3-EIRENE simulations, the neutral hydrogen pressure is typically $P_0 \sim 1.0$–2.0×10^{-6} mbar (corresponding to $n_H = 2.0$–4.0×10^{15} m^{-3}) at the SOL of the triangular plasma cross-section viewed by bolometers; it drops by two orders of magnitude in the plasma core down to $\sim 2.0 \times 10^{13}$ m^{-3} [41]. These n_H values are low, and no visible CX-effect is observed in STRAHL simulations. Therefore, we ignore the CX processes.

In the simulations, the Fe and C impurities are assumed to be released from the wall at a constant rate. The time of gas-puff turn-off, i.e. $t = 1.6$ s, is set as time = 0.0 s in the simulations. Throughout the simulation, we assume that the diffusion and convection parameters are not time-dependent and Fe and C impurities have the same transport coefficients.

4.2.2. The results. The diffusion coefficient and the convection parameter in equation (2) are free parameters for STRAHL, which are varied until a satisfactory reproduction of the radiation profile is obtained. The time response of the line-integrated SXR signal is followed as a further boundary condition. We select only the SXR channel that passes through the plasma center to ensure a sufficient signal-to-noise ratio.

Because of the sensitivity of the impurity radiation profile to the V^* profile (as shown above), we first obtain an initial guess for $V^*(r)$ by simulating the normalized radiation profile for $\rho < 0.5$ for a fixed diffusion coefficient D (e.g. 0.5 m^2 s^{-1})

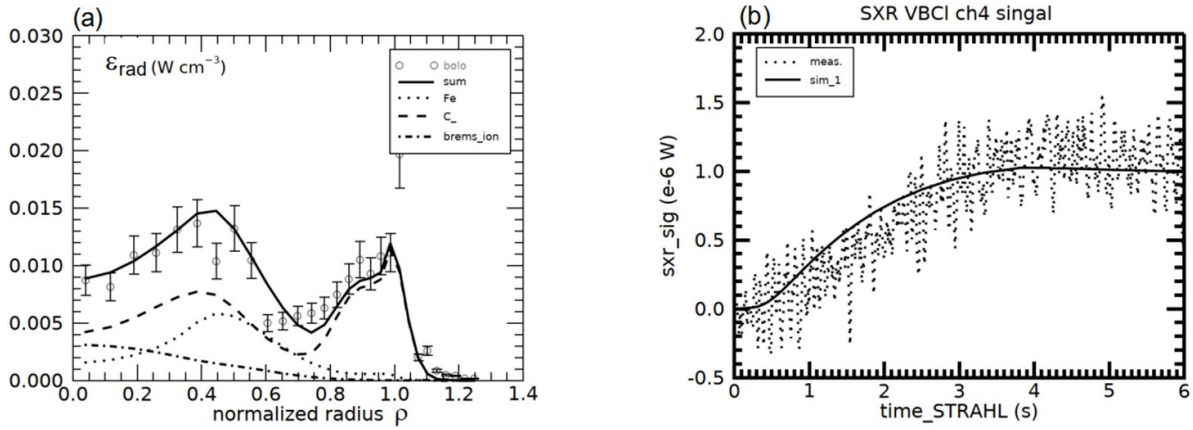

Figure 9. (a) The simulated impurity radiation profiles from C (dashed line) and Fe (dotted line) elements and their summation (solid line), which match the bolometer results (in circle); the dash-dotted line shows the plasma bremsstrahlung; (b) the simulated SXR signal (black line) and the measured one (dotted line). The determined transport coefficients, $D(r)$ and $V^*(r)$, are shown in figure 10.

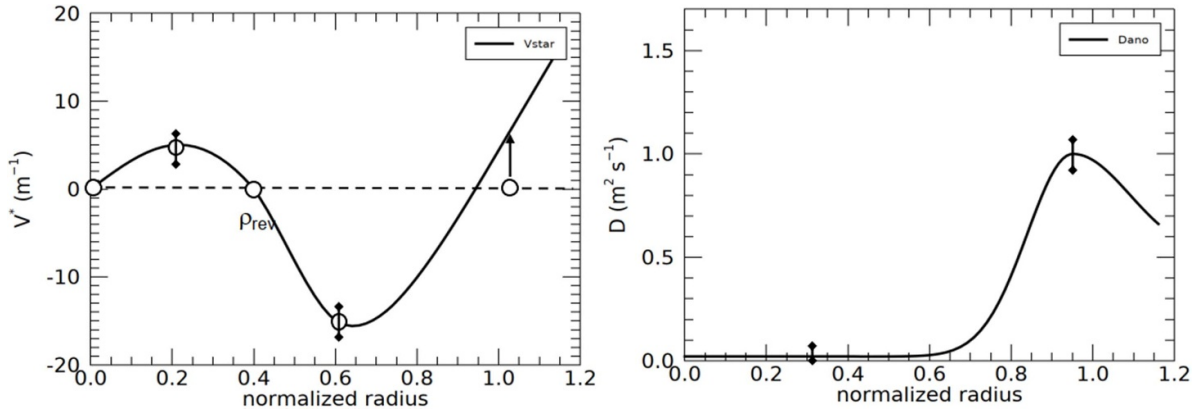

Figure 10. The obtained $V^*(r)$ (left) and $D(r)$ (right) profile by simulating the radiation profile and time evolution of the SXR signals (see figure 9); they characterize the impurity transport properties in the studied plasma with a low diffusion ($D(0) \sim 0.02$ m^2 s^{-1}) and a reversal of the convection around $\rho = \rho_{\rm rev} \sim 0.4$. The typical error bars in the V^* and the D-profile are shown.

by iteratively changing the node values. We then modify the *D(r)* profile while maintaining the derived *V*(r)* profile to change the SXR rise time. We expect anomalous transport in the outer plasma region ($\rho > 0.8$), where the temperature gradient is significantly higher than the density gradient (typically signaling ion temperature gradient (ITG) driven turbulence; see section 5.2). The D values at the edge can be adjusted by changing the peak value and the peak position (r_m), and a decay function is used around r_m; the decay width β is ∼8.0 cm, which is of the order of the gradient length (see figure 13 (right)).

Finally, the neutral Fe influx is set to a level ($\sim 2.0 \times 10^{19}$ s^{-1}) such that the Fe concentration is equal to the level estimated by the PHA system (see section 3.2); the neutral C influx is set to a level ($\Gamma_{0,C}$, $\sim 3.5 \cdot 10^{20}$ s^{-1}), such that the total radiation profile of C and Fe meet the values measured by the bolometer system. It is worth noting that both the D and V^* values at the edge affect the overall impurity (radiation) level as well as the profile at the edge; they are adjusted (along with the neutral impurity flux) in the final stage so that the impurity emission in the outer region also shows fair agreement with the experimental results. Figure 9 compares the experimental data with the best simulation result. The radiation from the Fe element (figure 9(a)) has a lower intensity than that from the C element due to the relatively lower inflow. The time evolution of the SXR channel signals from the simulation and experiment are summarized in figure 9(b); the simulation results are shown up to 6.0 s when the signal reaches a plateau representing the steady state. The obtained *D(r)* and *V*(r)* profiles are shown in figure 10. A low diffusion coefficient $D = 0.02$ m^2 s^{-1} is obtained for the inner plasma region ($\rho < 0.5$), necessary to reproduce the time trace of the SXR signal. Taking into account the signal uncertainty, the D-value derived has an uncertainty of ∼50%. An inversion of impurity convection at $\rho_{\rm rev} \sim 0.4$ is further obtained, i.e. with positive (outward) convection inside $\rho_{\rm rev}$ and negative (inward) convection outside $\rho_{\rm rev}$. The maximum normalized convection parameter is $V^*_m \sim -15.0$ m^{-1} corresponding to $V \sim -0.3$ m s^{-1} at $\rho \sim 0.6$ while $V^*_m \sim 5.0$ m^{-1} corresponding to $V \sim 0.1$ m s^{-1} at $\rho \sim 0.2$; they have an uncertainty of ∼20%–40%.

The radial distributions of the density of the individual impurity ions, their emissions, and the SXR fraction are shown in figure 11, (a)–(c) for the C impurity and (d)–(f) for the

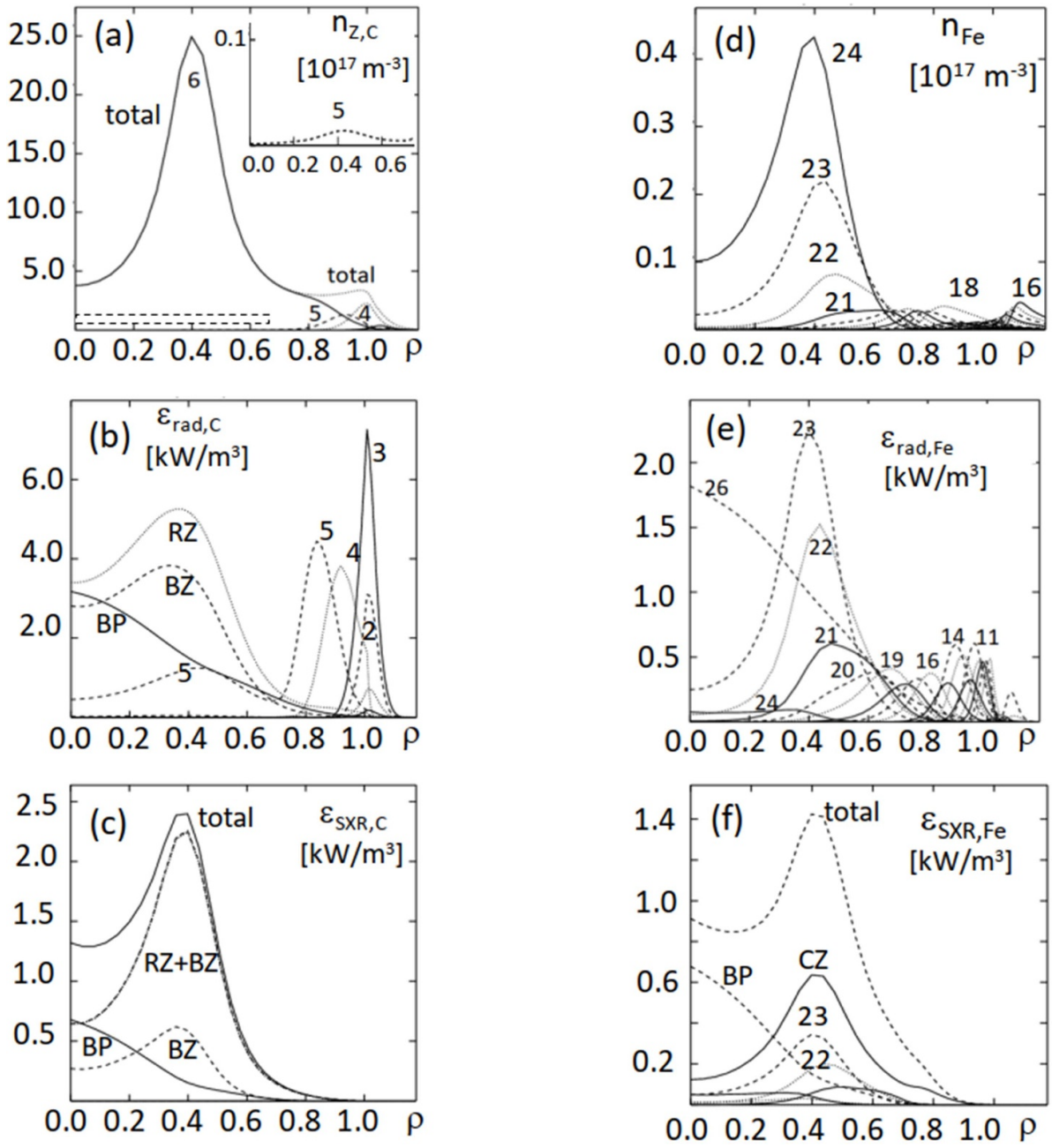

Figure 11. The STRAHL simulation results for C (a)–(c) and Fe (d)–(f) ions (denoted by charge state Z) in the HP phase in XP7: (a) and (d) the impurity ion density profile; (b) and (e) the emission profile for selected ions and (c) and (f) the SXR radiation profile. The inset in (a) shows the CVI density profile in the inner plasma region with $\rho < 0.6$. The contributions from the continuum radiation due to impurity ion recombination (RZ), main plasma bremsstrahlung (BP), and impurity bremsstrahlung (BZ) are also shown.

Fe impurity. It can be clearly seen that near the radial position of the emission maximum ($\rho \sim 0.4$), the impurity density due to the highly charged C ions ($Z = 5$–6) and Fe ions (e.g. $Z = 22$–24) is at its maximum. The profile of the total impurity density, which is the sum of all impurity ions, will also peak at $\rho \sim 0.4$, which is clearly different from the monotonic decrease of the n_e profile, as shown in figure 4(c), confirming the local impurity accumulation. The FeXXV ($Z = 24$), with an ionization potential of about 1.9 keV, exhibits the highest concentration and a broader distribution, yet the lower-charged states with $Z = 22$–23 have stronger line emission (see figures 11(d) and (e)). The CVI ($Z = 5$) density is normally (no inward convection) located in the outer plasma region, but now apparently contribute to the local C radiation (see figure 11(b)) in spite of its low density there (see inset in figure 11(a)).

Note that the radially averaged $Z_{\rm eff}$ value is ∼1.6 from the simulations matching the experimental results; its local value varies radially with a peak value of ∼2.2 at $\rho_m = 0.4$. Furthermore, we note that the impurity density around the plasma axis is lower than the peak value (at ρ_m) by a factor of 4–5, indicating a central impurity 'hole'. These observations

are similar to those observed at LHD [61], where outward impurity convection has played a key role in 'pumping' the impurities out of the plasma center.

The simulations have also been performed for the HP phase in XP5. The determined D and V values in the inner plasma region are close to those for XP7, apart from the convection reversal position, which is at $\rho = 0.3$, corresponding to the emission peak position in figure 6(a). The detailed simulations are not shown here.

5. Discussions about collisional impurity transport and turbulence suppression

The low diffusion level and the prominent convective parameter derived above suggests that (neo-)classical impurity transport (categorized as collisional) might play a key role here. This neo-classical effect could become relevant after the turbulence transport is suppressed.

5.1. The collisional impurity transport

5.1.1. The neoclassical transport. In the frame of the stellarator-specific neoclassical transport, the impurity flux is strongly dependent on the magnetic topology and the radial electric field E_r in addition to the various thermodynamic forces [62, 63]. The diffusive and convective transport coefficient for the impurity ion are given by

$$D_{\rm neo} = D_1^z, \tag{6}$$

$$V_{\rm neo} = D_1^z \left(\frac{q_z E_r}{T_z} - \left(\frac{D_2^z}{D_1^z} - \frac{3}{2} \right) \frac{1}{T_z} \frac{{\rm d}T_z}{{\rm d}r} \right), \tag{7}$$

where, D_1^z and D_2^z are neoclassical transport coefficients given by the energy integration of the mono-energetic particle diffusion coefficients $D_{\rm mono}$ as

$$D_1^z = \frac{2}{\sqrt{\pi}} \int_0^\infty D_{\rm mono}(X)\, e^{-X} X^{0.5} {\rm d}X,$$

$$D_2^z = \frac{2}{\sqrt{\pi}} \int_0^\infty D_{\rm mono}(X)\, e^{-X} X^{1.5} {\rm d}X,$$

where $X = mv^2/2\ T$, m and v are the mass and the velocity of the ion species, $T = T_i = T_z$, and q_z is its charge. $D_{\rm mono}$ is obtained from the DKES code [64] and depends on collisionality, electric field and magnetic topology. Negative $V_{\rm neo}$ values are normally associated with the ion-root ($E_{\rm r} < 0$), which determines the inward convection of the impurity ions, while the outward convection is normally associated with the electron-root ($E_{\rm r} > 0$) in the plasma center.

The experimental $E_{\rm r}$ profile is derived from the XICS measurements in the HP phase in XP7 (no $E_{\rm r}$ data available for XP5) and is presented in figure 12. This radial electric field is inferred from XICS measurements of the perpendicular velocity through the radial force-balance equation [65]. The results

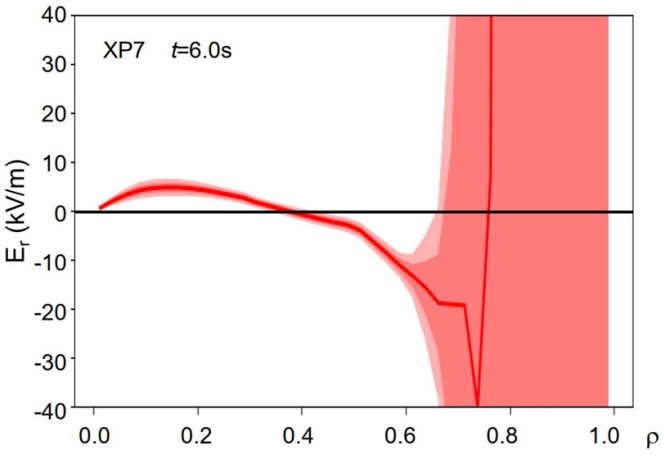

Figure 12. The $E_{\rm r}$-profile in the HP-phase in XP7 ($t = 6.0$ s) obtained from the XICS diagnostic. The uncertainty of the results is shadowed.

are subject to larger uncertainties in the outer plasma region ($\rho > 0.6$), while in the inner plasma area, they clearly show a transition from an e-root to an ion-root at $\rho \sim 0.4$, which agrees with the position of the sign reversal of the convection V^* in figure 10 (left). The correlation between the convection and the electric field (see equation (7)) can then be observed experimentally. The $E_{\rm r}$ value in the e-root is low with a magnitude of $\sim$5 kV m^{-1} (having an uncertainty of $\sim$2 kV m^{-1}).

We have calculated the theoretical neoclassical $E_{\rm r}$ values based on the ambipolar condition of the neoclassical radial electron and ion fluxes. The $T_{\rm e}-$, $n_{\rm e}-$ profiles used are those shown in figures 4(c) and (d) ($t = 6.0$ s; in green); as with the $T_{\rm i}$ data, the central values (for $\rho \leqslant 0.4$) are taken from the XICS system, and beyond this range where $T_{\rm i} > T_{\rm e}$ occurs, we assume $T_{\rm i} = T_{\rm e}$ (see section 3.1). The calculated $E_{\rm r}$ values show a general ion-root with $E_{\rm r} = -9.0$ kV m^{-1} at $\rho \sim 0.6$, which is close to the measured one. Nevertheless, the e-root in the plasma center is not obtained. We suspect that this is due to the uncertainties in the profiles, for instance, slightly reducing the $n_{\rm e}$ values by $\sim$10% and additionally flattening the $T_{\rm i}$ profile in the inner region could result in an e-root solution having a magnitude comparable to that measured by the XICS system.

5.1.2. The classical transport. The classical contribution is associated with the collisionality and the magnetic field strength, but is independent of the $E_{\rm r}$ values. The diffusive and convective transport coefficient for the impurity ion with a charge state Z are expressed as

$$D_{z,cl} = T_z \frac{m_z}{Z^2 e^2} \sum_b \nu_{zb} \left(1 + \frac{m_z}{m_b} \right)^{-1/2} \left\langle \frac{|\nabla \Psi|^2}{B^2} \right\rangle, \tag{8}$$

$$V_{z,cl} = D_z Z \left\{ \frac{{\rm d}\ln(n_i)}{{\rm d}r} - \frac{1}{2} \frac{{\rm d}\ln T_i}{{\rm d}r} \right\}, \tag{9}$$

here m_z and m_i are the impurity and main ion mas, ν_{iz} is the proton-impurity collision frequency, and $m_z \gg m_i$ and

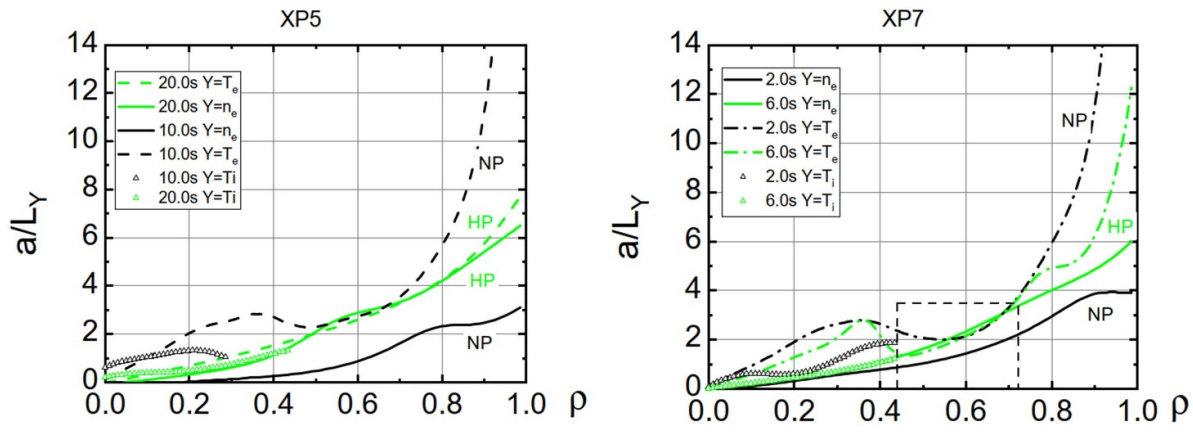

Figure 13. The normalized gradients of n_e, T_e, and T_i (in the inner plasma region) for the NP and HP phases in XP5 (left) and XP7 (right). A similarity is observed between a/L_{Ti} and a/L_{ne} in the HP phase, exemplified in the middle radial region by the dashed frame for XP7.

$Z \gg 1$ are assumed. These classical terms, usually ignored, may become more important under the real plasma conditions, as expected for the neo-classically optimized W7-X stellarator (see [66]).

We have estimated both the neoclassical and classical transport coefficients (given as D_{neo} and D_{cl}) and the convective transport coefficients (given as V_{neo} and V_{cl}) for Fe^{24+} and C^{6+}. The main results are (1) the total diffusion coefficient, $D_{neo} + D_{cl}$, for both impurity ions is ~0.01–0.02 $m^2\ s^{-1}$ in the inner plasma region; (2) the value of the total (inward) convective coefficients $|V_{neo} + V_{cl}|$ is ~0.3–0.5 $m\ s^{-1}$ at $\rho \sim 0.6$. Both are close to the values derived from STRAHL simulations. However, no outward convection is achieved in the neoclassical term, since the neoclassical solution did not have an electron root. As mentioned above, we suspect that the reason lies in profile uncertainties.

Note that for the Fe^{24+} ions, the classical term dominates (e.g. the value of D_{CL} is higher than that of D_{neo} by a factor of ~5); an outward convection $V_{CL} > 0$ is obtained at the plasma center ($\rho < 0.3$).

5.2. Considerations of mechanisms to suppress turbulent transport in the HP-phases

With the experiences gained in density peaking scenarios in W7-X (such as after pellet injections) [25, 67], we expect a reduced heat and particle turbulent transport in the HP-phases of the studied plasmas. This translates in a higher confinement time for main plasma ions and impurities. Since diagnostics that normally provide information on density fluctuations are not available, we investigate profile gradients, considering that both density and temperature gradients are determinants of ITG turbulence in both tokamak and stellarator plasmas [68, 69].

The relative gradient length, defined as a/L_Y with $L_Y = -(\mathrm{dln}Y/\mathrm{d}r)^{-1}$ for the gradient length of parameter Y (such as n_e, T_e, and T_i) and a for the smaller radius of the plasma, is calculated using the fits of the profiles in figure 4. Note that for the calculation of L_{Ti}, we use the T_i value from the XICS for the inner plasma region while we assume $T_i = T_e$ for the outer region (the reason has already been described in section 3.1). The results for the NP and HP phases in XP5 and XP7 are shown in figure 13 (left) and (right), respectively. It can be seen that the value of a/L_{ne} for the HP phases (in solid greed line) increases monotonically with radial position; it is close to that of a/L_{Ti}, i.e. the ratio $\eta_i = (a/L_{Ti})/(a/L_{ne}) \sim 1$, for most of the plasma region ($\rho < 0.7$–0.8). In contrast, the values of η_i for the NP phases are generally higher.

In the following, we combine our results with the stability map [70] describing the growth rate of electrostatic micro-instabilities associated with turbulent transport. Figure 14 replots the growth rates for the hydrogen W7-X plasma in the high-iota magnetic configuration as a function of a/L_{Ti} and a/L_{ne} (cf figure 5(a) in [70]). They have been obtained by linear gyro-kinetic simulations of micro-instabilities at ion scales, i.e. $k_\perp \rho_i \simeq 1$ with $k_\perp$ standing for the mode wavelength and ρ_i for the ion gyro-radius, using the GENE code [71]. This map is characterized by three distinct regions: (1) on the top-left, where the ITG is the dominant instability with $a/L_{Ti} > a/L_{ne}$; (2) on the bottom-right, where the TEM (trapped electron mode) is the dominant one with $a/L_{ne} > a/L_{Ti}$ (driven by density-gradient); (3) a region along the main diagonal, with $\eta_i \sim 1$, where the linear growth rate γ is significantly reduced or close to zero.

According to the map, the instability level for different plasma phases in the studied plasma can be assessed from the values of a/L_{Ti} and a/L_{ne} in figure 13. The values for the selected radial positions at $\rho = 0.3$, 0.6, 0.8, and 0.9 are now marked in the map by asterisks and pentagons for XP5 and XP7, respectively, and in green and black for the respective HP and NP phases.

It can be seen that (1) most of the green symbols are located in the stability valley, especially those for the HP phase in XP5, the values of a/L_{ne} and a/L_{Ti} are in agreement with the conditions of the stability valley for the reduction of turbulence; in XP7, the points for the inner region are well located in the valley, while those for the outer region ($\rho = 0.8$ and 0.9) are located at the border of the valley. The preliminary simulations show that a mixed ITG-TEM mode dominates the turbulence. (2) For the NP phases in both plasmas (see black symbols),

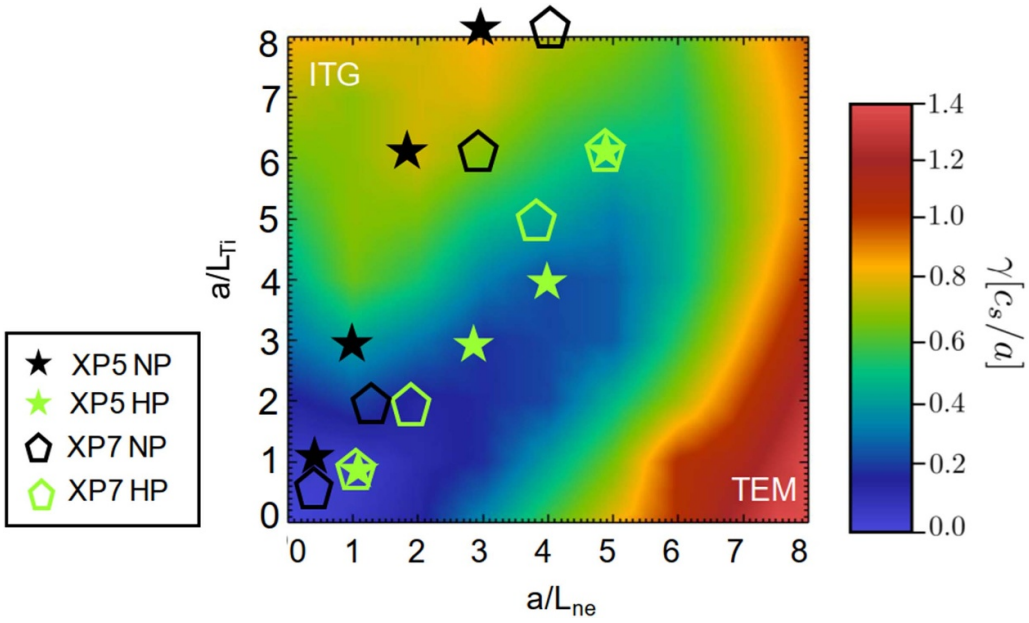

Figure 14. The 2D stability map for the hydrogen W7-X plasma in high-iota magnetic configuration shows the micro-instability growth rate (see the color bar) as a function of a/L_{ne} and a/L_{Ti}. The values of a/L_{ne} and a/L_{Ti} at $\rho = 0.3$, 0.6, 0.8, and 0.9 for the both NP and HP phases in XP5 and XP7 are marked by stars and pentagons. Note that the value of a/L_{Ti} at $\rho = 0.9$ is $\sim$12 for both discharges, which exceeds the range of the Y-axis.

the ITG turbulence is the dominant instability, especially for the outer radial positions (with $a/L_{Ti} \geqslant 6$ and $a/L_{ne} \leqslant 4$). It is noteworthy that the growth rates in the plasma core ($\rho = 0.3$) are also low for the NP phases; both a/L_{ne} and a/L_{Ti} are small ($\leqslant 1$) and are placed in the stability valley.

The stability valley predicted for the W7-X plasma in the high-iota configuration, which occurs when the normalized temperature and density gradients are similar, i.e. $\eta_i \approx 1$, is now observed experimentally in the HP phases of XP5 and XP7. The turbulence transport in the NP phase is dominated by the ITG mode, especially in the outer plasma region.

Note that the influence of the η_i value on the turbulence transport in the W7-X plasma is also experimentally described in [52], however with higher values.

6. Conclusion

At Wendelstein 7-X, an enrichment of impurities in the inner plasma region has been observed for the first time in ECR-heated hydrogen plasmas (no pellet injections) with a power of 0.6 MW and 1.2 MW. This is evidenced by profiles of radiated power with a pronounced radiation zone in the inner plasma region (peaking at $\rho_m = 0.3$–0.4) and the spectroscopic measurements showing an associated increase of high-Z elements such as Fe. Analysis of impurity transport under realistic plasma conditions has revealed (1) a low diffusion of $D \sim 0.02$ m^2 s^{-1} for the inner plasma region ($\rho < 0.5$), which is significantly lower than the normal turbulent diffusion transport (by a factor of $\sim$10) and comparable to that predicted by classical and neo-classical theory; (2) a reversal of impurity transport convection at the radial position near the radiation maximum: inside with positive (outward) convection ($|V| \sim 0.1$ m s^{-1}) and outside with negative (inward) convection ($|V| \sim 0.3$ m s^{-1}). Accumulation of the impurity ions around the radiation maximum is confirmed. The magnitude of inward convection determined at half the plasma radius is close to the theoretical prediction, but outward convection at inner radii is not reproduced by the theory because the neo-classical ambipolar solution does not have a central electron root. The reason for this discrepancy is probably due to profile uncertainties.

Despite the impurity accumulation, the plasma phase exhibits enhanced energy confinement; the transition from a normal-performance phase to this high-performance phase occurs when the gas supply is turned off, which reduces the edge plasma density ($<1.0 \times 10^{19}$ m^{-3}), resulting in a steepening of the density profile; moreover, the density and temperature gradient lengths are similar, with a ratio $\eta_i = (a/L_{Ti})/(a/L_{ne}) \sim 1$, corresponding to the 'stability valley' conditions for micro-instability reduction. In contrast, in the NP phases, especially in the outer plasma region, the ITG turbulence represents the dominating instability.

Finally, we note that the compatibility of impurity accumulation and enhanced energy confinement is likely due to the generally low impurity levels (e.g. the averaged value of Z_{eff} is <2, and Fe concentrations are $\lesssim 10^{-4}$).

Data availability statement

All data that support the findings of this study are included within the article (and any supplementary files).

Acknowledgments

This work has been carried out within the framework of the EUROfusion Consortium, funded by the European Union via the Euratom Research and Training Programme (Grant Agreement No 101052200—EUROfusion). Views and opinions expressed are however those of the author(s) only and do not necessarily reflect those of the European Union or the European Commission. Neither the European Union nor the European Commission can be held responsible for them. Gyrokinetic simulations have been conducted on the Marconi supercomputer (CINECA, Italy) and on the Raven supercomputer (Garching, Germany). This scientific paper has been published as part of the international project co-financed by the Polish Ministry of Science and Higher Education within the programme called 'PMW' for 2022 under the Contract No. 5246/HEU-Euratom/2022/2.

ORCID iDs

D Zhang https://orcid.org/0000-0002-5800-4907
B Buttenschön https://orcid.org/0000-0002-9830-9641
M Kubkowska https://orcid.org/0000-0003-1320-7468
J A Alcusón https://orcid.org/0000-0001-5492-7432
C D Beidler https://orcid.org/0000-0002-4395-239X
M N A Beurskens https://orcid.org/0000-0002-3354-0279
A Langenberg https://orcid.org/0000-0002-2107-5488
N Pablant https://orcid.org/0000-0001-6617-8459
K Rahbarnia https://orcid.org/0000-0002-5550-1801
Th Wegner https://orcid.org/0000-0003-0136-0406
G Wurden https://orcid.org/0000-0003-2991-1484
S A Bozhenkov https://orcid.org/0000-0003-4289-3532
Y Feng https://orcid.org/0000-0002-3846-4279
K J Brunner https://orcid.org/0000-0002-0974-0457
Y Gao https://orcid.org/0000-0001-8576-0970
J Geiger https://orcid.org/0000-0003-4268-7480
L Giannone https://orcid.org/0000-0001-5611-200X
T Kremeyer https://orcid.org/0000-0002-6383-944X
S Kwak https://orcid.org/0000-0001-7874-7575
A Pavone https://orcid.org/0000-0003-2398-966X

References

[1] Ran L *et al* 1989 Impurity accumulation in plasma regimes with high energy confinement *J. Nucl. Mater.* **162** 14–23
[2] Wagner F 2018 The history of research into improved confinement regimes *Eur. Phys. J.* H **43** 523–49
[3] Wade M, Houlberg W and Baylor L 2000 Experimental confirmation of impurity convection driven by the ion-temperature gradient in toroidal plasmas *Phys. Rev. Lett.* **84** 282
[4] Giannone L *et al* 2003 Bolometer tomography at the density limit of the HDH mode in the W7-AS stellarator *Plasma Phys. Control. Fusion* **45** 1713
[5] Peterson B *et al* 2001 Multifaceted asymmetric radiation from the edge-like asymmetric radiative collapse of density limited plasmas in the large helical device *Phys. Plasmas* **8** 3861–4
[6] Burhenn R *et al* 2009 On impurity handling in high performance stellarator/heliotron plasmas *Nucl. Fusion* **49** 065005
[7] Maaßberg H, Beidler C and Simmet E 1999 Density control problems in large stellarators with neoclassical transport *Plasma Phys. Control. Fusion* **41** 1135
[8] Maassberg H, Burhenn R, Gasparino U, Kühner G, Ringler H and Dyabilin K S 1993 Experimental and neoclassical electron heat transport in the LMFP regime for the stellarators W7-A, L-2, and W7-AS *Phys. Fluids* B **5** 3627–40
[9] Pablant N *et al* 2018 Core radial electric field and transport in Wendelstein 7-X plasmas *Phys. Plasmas* **25** 022508
[10] Beidler C *et al* 2021 Demonstration of reduced neoclassical energy transport in Wendelstein 7-X *Nature* **596** 221–6
[11] Geiger B *et al* 2019 Observation of anomalous impurity transport during low-density experiments in W7-X with laser blow-off injections of iron *Nucl. Fusion* **59** 046009
[12] Langenberg A *et al* 2020 Charge-state independent anomalous transport for a wide range of different impurity species observed at Wendelstein 7-X *Phys. Plasmas* **27** 052510
[13] Wegner T, Bähner J-P, Buttenschön B, Langenberg A and von Stechow A 2023 Overview of core impurity transport in the first divertor operation of Wendelstein 7-X *J. Plasma Phys.* **89** 955890302
[14] Yamada H *et al* 2005 Characterization of energy confinement in net-current free plasmas using the extended international stellarator database *Nucl. Fusion* **45** 1684
[15] Fuchert G *et al* 2020 Increasing the density in Wendelstein 7-X: benefits and limitations *Nucl. Fusion* **60** 036020
[16] Beurskens M N *et al* 2021 Ion temperature clamping in Wendelstein 7-X electron cyclotron heated plasmas *Nucl. Fusion* **61** 116072
[17] Ford O P *47th EPS Plasma Physics Conf.* (*Sitges, Spain*, 2020/1)
[18] Zhang D *et al* 2019 First observation of a stable highly dissipative divertor plasma regime on the Wendelstein 7-X stellarator *Phys. Rev. Lett.* **123** 025002
[19] Schmitz O *et al* 2020 Stable heat and particle flux detachment with efficient particle exhaust in the island divertor of Wendelstein 7-X *Nucl. Fusion* **61** 016026
[20] Jakubowski M *et al* 2021 Overview of the results from divertor experiments with attached and detached plasmas at Wendelstein 7-X and their implications for steady-state operation *Nucl. Fusion* **61** 106003
[21] Pedersen T S *et al* 2019 First divertor physics studies in Wendelstein 7-X *Nucl. Fusion* **59** 096014
[22] Zhang D *et al* 2021 Bolometer tomography on Wendelstein 7-X for study of radiation asymmetry *Nucl. Fusion* **61** 116043
[23] Zhang D *et al* 2022 *Compatibility of high-Z impurity accumulation with high plasma performance in ECR-heated W7-X plasmas 48th EPS Conf. on Plasma Physics*
[24] Klinger T *et al* 2019 Overview of first Wendelstein 7-X high-performance operation *Nucl. Fusion* **59** 112004
[25] Bozhenkov S *et al* 2020 High-performance plasmas after pellet injections in Wendelstein 7-X *Nucl. Fusion* **60** 066011
[26] Baldzuhn J *et al* 2020 Enhanced energy confinement after series of pellets in Wendelstein 7-X *Plasma Phys. Control. Fusion* **62** 055012
[27] Behringer K 1987 *JET Report JET-R (87) 08* (Joint European Torus)
[28] Dux R 2006 *STRAHL user manual*
[29] Behringer K 1987 *Description of the Impurity Transport Code'straHl'* Commission of the European Communities

[30] Wolf R *et al* 2019 Performance of Wendelstein 7-X stellarator plasmas during the first divertor operation phase *Phys. Plasmas* **26** 082504

[31] Pedersen T S *et al* 2018 First results from divertor operation in Wendelstein 7-X *Plasma Phys. Control. Fusion* **61** 014035

[32] Wegner T *et al* 2018 Design, capabilities, and first results of the new laser blow-off system on Wendelstein 7-X *Rev. Sci. Instrum.* **89** 073505

[33] Bussiahn R, Tamura N, McCarthy K J, Burhenn R, Hayashi H, Laube R and Klinger T 2018 Tracer-encapsulated solid pellet (TESPEL) injection system for Wendelstein 7-X *Rev. Sci. Instrum.* **89** 10K112

[34] Zhang D *et al* 2010 Design criteria of the bolometer diagnostic for steady-state operation of the W7-X stellarator *Rev. Sci. Instrum.* **81** 10E134

[35] Zhang D *et al* 2014 Feasibility assessment of bolometry as impurity transport study tool for the stellarator W7-X *41st EPS Conf. on Plasma Physics*

[36] Biel W and team T 2005 Vacuum ultraviolet spectroscopy at TEXTOR *Fusion Sci. Technol.* **47** 246–52

[37] Kubkowska M *et al* 2018 Plasma impurities observed by a pulse height analysis diagnostic during the divertor campaign of the Wendelstein 7-X stellarator *Rev. Sci. Instrum.* **89** 10F111

[38] Jabłoński S, Czarnecka A, Kubkowska M, Ryć L, Weller A, Biedermann C and König R 2015 Simulation of pulse height analysis soft x-ray spectra expected from W7-X *J. Instrum.* **10** P10021

[39] Pavone A *et al* 2019 Measurements of visible bremsstrahlung and automatic Bayesian inference of the effective plasma charge Zeff at W7-X *J. Instrum.* **14** C10003

[40] Ford O *et al* 2020 Charge exchange recombination spectroscopy at Wendelstein 7-X *Rev. Sci. Instrum.* **91** 023507

[41] Winters V *et al* 2021 EMC3-EIRENE simulation of first wall recycling fluxes in W7-X with relation to H-alpha measurements *Plasma Phys. Control. Fusion* **63** 045016

[42] Haak V, Bozhenkov S A, Feng Y, Kharwandikar A, Kremeyer T, Naujoks D, Perseo V, Schlisio G and Wenzel U 2023 Overview over the neutral gas pressures in Wendelstein 7-X during divertor operation under boronized wall conditions *Plasma Phys. Control. Fusion* **65** 055024

[43] Rahbarnia K *et al* 2018 Diamagnetic energy measurement during the first operational phase at the Wendelstein 7-X stellarator *Nucl. Fusion* **58** 096010

[44] Pasch E, Beurskens M N A, Bozhenkov S A, Fuchert G, Knauer J and Wolf R C 2016 The Thomson scattering system at Wendelstein 7-X *Rev. Sci. Instrum.* **87** 11E729

[45] Bozhenkov S A *et al* 2017 The Thomson scattering diagnostic at Wendelstein 7-X and its performance in the first operation phase *J. Instrum.* **12** P10004

[46] Hirsch M *et al* 2019 ECE diagnostic for the initial operation of Wendelstein 7-X *EPJ Web Conf.* **203** 03007

[47] Hoefel U *et al* 2019 Bayesian modeling of microwave radiometer calibration on the example of the Wendelstein 7-X electron cyclotron emission diagnostic *Rev. Sci. Instrum.* **90** 043502

[48] Langenberg A *et al* 2018 Prospects of x-ray imaging spectrometers for impurity transport: recent results from the stellarator Wendelstein 7-X *Rev. Sci. Instrum.* **89** 10G101

[49] Zohm H 1996 Edge localized modes (ELMs) *Plasma Phys. Control. Fusion* **38** 105

[50] Chaudhary N *et al* 2023 Radial localization of electron temperature pedestal and ELM-like events using ECE measurements at Wendelstein 7-X *EPJ Web Conf.* **277** 03004

[51] Wurden G A *et al* 2022 A special case of long-pulse high performance operation in W7-X *EPS Plasma Physics Conf.* p 1b.118

[52] Carralero D *et al* 2021 An experimental characterization of core turbulence regimes in Wendelstein 7-X *Nucl. Fusion* **61** 096015

[53] Zhang D *et al* 2021 Plasma radiation behavior approaching high radiation scenarios at W7-X *28th IAEA Fusion Energy Conf. (FEC2020)* (Vitual Event)

[54] Summers H and McWhirter R 1979 Radiative power loss from laboratory and astrophysical plasmas. I. Power loss from plasmas in steady-state ionisation balance *J. Phys. B: At. Mol. Phys.* **12** 2387

[55] Feng Y *et al* 1997 A 3D Monte Carlo code for plasma transport in island divertors *J. Nucl. Mater.* **241** 930–4

[56] Mollén A, Landreman M, Smith H M, García-Regaña J M and Nunami M 2018 Flux-surface variations of the electrostatic potential in stellarators: impact on the radial electric field and neoclassical impurity transport *Plasma Phys. Control. Fusion* **60** 084001

[57] García-Regaña J *et al* 2017 Electrostatic potential variation on the flux surface and its impact on impurity transport *Nucl. Fusion* **57** 056004

[58] Braun S and Helander P 2010 Pfirsch–Schlüter impurity transport in stellarators *Phys. Plasmas* **17** 072514

[59] Fussmann G 1986 Analytical modelling of impurity transport in toroidal devices *Nucl. Fusion* **26** 983

[60] Dux R, Giroud C and Zastrow K-D 2004 Impurity transport in internal transport barrier discharges on JET *Nucl. Fusion* **44** 260

[61] Ida K *et al* 2009 Observation of an impurity hole in a plasma with an ion internal transport barrier in the large helical device *Phys. Plasmas* **16** 056111

[62] Beidler C *et al* 2011 Benchmarking of the mono-energetic transport coefficients—results from the international collaboration on neoclassical transport in stellarators (ICNTS) *Nucl. Fusion* **51** 076001

[63] Igitkhanov Y, Polunovsky E and Beidler C 2006 Impurity dynamics in nonaxisymmetric plasmas *Fusion Sci. Technol.* **50** 268–75

[64] Van Rij W and Hirshman S 1989 Variational bounds for transport coefficients in three-dimensional toroidal plasmas *Phys. Fluids* B **1** 563–9

[65] Pablant N *et al* 2020 Investigation of the neoclassical ambipolar electric field in ion-root plasmas on W7-X *Nucl. Fusion* **60** 036021

[66] Buller S, Mollén A, Newton S L, Smith H M and Pusztai I 2019 The importance of the classical channel in the impurity transport of optimized stellarators *J. Plasma Phys.* **85** 175850401

[67] Stechow A V *et al* 2020 Suppression of core turbulence by profile shaping in Wendelstein 7-X (arXiv:2010.02160)

[68] Xanthopoulos P, Mynick H, Helander P, Turkin Y, Plunk G, Jenko F, Görler T, Told D, Bird T and Proll J 2014 Controlling turbulence in present and future stellarators *Phys. Rev. Lett.* **113** 155001

[69] Horton W 1999 Drift waves and transport *Rev. Mod. Phys.* **71** 735

[70] Alcusón J, Xanthopoulos P, Plunk G G, Helander P, Wilms F, Turkin Y, Stechow A V and Grulke O 2020 Suppression of electrostatic micro-instabilities in maximum-J stellarators *Plasma Phys. Control. Fusion* **62** 035005

[71] Jenko F, Dorland W, Kotschenreuther M and Rogers B N 2000 Electron temperature gradient driven turbulence *Phys. Plasmas* **7** 1904–10